Conditioning of unsteady cross-flow instability modes using dielectric barrier discharge plasma actuators

Serpieri, Jacopo; Kotsonis, Marios

DOI
10.1016/j.expthermflusci.2018.01.007

Publication date
2018

Document Version
Accepted author manuscript

Published in
Experimental Thermal and Fluid Science

Conditioning of unsteady cross-flow instability modes using dielectric barrier discharge plasma actuators

Jacopo Serpieri[1] and Marios Kotsonis
AWEP Department, Section of Aerodynamics, TU Delft,
Kluyverweg 1, 2629HS Delft, The Netherlands

Abstract

In this study, experiments are performed towards the identification and measurement of unsteady modes occurring in a transitional swept wing boundary layer. These modes are generated by the interaction between the primary stationary and travelling cross-flow instabilities or by secondary instability mechanisms of the stationary cross-flow vortices and have a crucial role in the laminar-to-turbulent breakdown process. Detailed hot-wire measurements were performed at the location of stationary instability amplitude-saturation. In order to deterministically capture the spatio-temporal evolution of the unsteady modes, measurements were phase- and frequency-conditioned using concurrent forcing by means of a dielectric barrier discharge plasma actuator mounted upstream of the measurement domain. The actuator effect, when positioned sufficiently upstream the secondary modes onset, was tuned such to successfully condition the high-frequency *type-I* and the low-frequency *type-III* modes without modifying the transition evolution. Two primary stationary cross-flow vortices of different amplitude were measured, revealing the effect of base-flow variations on the growth of travelling instabilities. The response of these two stationary waves to the naturally occurring and forced fluctuations was captured at different chordwise positions. Additionally, the deterministic conditioning of the instability phase to the phase of the actuation allowed phase-averaged reconstruction of the spatio-temporal evolution of the unsteady structures providing valuable insight on their topology. Finally, the effect of locating the actuator at a more downstream position, closer to the secondary instability branch-I, resulted in laminar-to turbulent breakdown for the high-frequency actuation while the low-frequency forcing showed milder effects on the transition evolution.

Keywords: laminar-to-turbulent transition, cross-flow instability, swept wing, plasma actuator

Symbols

A	Amplitude
b	Wing span in the Z direction
c	Wing chord in the x direction
c_X	Wing chord in the X direction
C_μ	Actuator momentum coefficient
C_p	Pressure coefficient
d	Roughness elements diameter
E	Voltage amplitude
f	Frequency
k	Roughness elements height
M	Optical magnification
Re	Free-stream Reynolds number
t	Time
T	Actuator thrust in the wall-parallel direction
Tu	Turbulence intensity
u, v, w	Velocity component along the x, y, z directions
U, V, W	Velocity along the X, Y, Z directions
x, y, z	Wing coordinates
x_t, y_t, z_t	Wing surface coordinates
X, Y, Z	Wind-tunnel coordinates
α	Angle of attack, wavenumber
γ	Angle of the inviscid streamline w.r.t x
δ_f	Spectral frequency resolution
ϑ	Momentum-loss thickness
λ	Wavelength
Λ	Sweep angle
ν	Kinematic viscosity
ϱ	Air density
Φ	Phase
ω	Angular frequency
$\bar{...}$	Time-average
$\{...\}$	Standard deviation w.r.t. the subscript quantity
$...'$	Fluctuations
$\lvert...\rvert$	Magnitude

Sub/super-scripts

co	Cut-off
e	At the boundary layer edge
DBD	Related to the actuator
s	Sampling
m	At the maximum extent
I	Related to stationary modes
II	Related to unsteady modes

∞	Free-stream quantity
Φ	Related to phases
0	Reference value

Abbreviations

AC-DBD	Alternating Current Dielectric Barrier Discharge
CE	Covered Electrode
CF	Cross-Flow
CFV	Cross-Flow Vortices
CTA	Constant Temperature Anemometer
DNS	Direct Numerical Simulation
DRE	Distributed Roughness Element
EE	Exposed Electrode
EMI	Electromagnetic Interference
HF	High Frequency
HWA	Hot-Wire Anemometry
KH	Kelvin-Helmholtz
LF	Low Frequency
POD	Proper Orthogonal Decomposition
PR	Phase Reconstructed
PSD	Power Spectral Density
TS	Tollmien-Schlichting

1. Introduction

1.1. Background

Swept wings and axisymmetric bodies at incidence or rotating about their axis feature three-dimensional streamlines. Within the boundary layer, the flow experiences an imbalance between pressure and inertial forces and tends to be torn by the pressure gradient. This phenomenon causes a secondary flow called *cross-flow* (CF), which leads to inviscidly unstable boundary layers. In low free-stream turbulence environments, this instability manifests in stationary co-rotating vortices (the so-called cross-flow vortices (CFVs)), approximately aligned with the flow [2, 29]. These cross-flow vortices, although weak disturbances of the wall-normal and spanwise velocity components, deeply modify the base-flow boundary layer by displacing low-momentum air upwards towards the outer edges of the boundary layer and vice-versa, thus causing a strong modification of the spatial arrangement of the streamwise velocity [1, 2]. Strong velocity gradients along the wall normal and spanwise directions appear in the transitional boundary layer, giving rise to the development and amplification of Kelvin-Helmholtz (KH) type instability modes [3]. Two different travelling modes (*type-I* and *type-II*) have been individuated and named after their locations with respect to the streamwise velocity gradients as *z-mode* and *y-mode*, respectively [22]. These two modes feature very high frequencies and explosive spatial amplifications. Malik et al. [21] and White and Saric [38] reported a third region of strong fluctuations related to the interaction between the primary travelling cross-flow waves and the stationary CF vortices. Fischer and Dallmann [10], Högberg and Henningson [13], Wassermann and Kloker [35], Bonfigli and Kloker [3] interpreted these fluctuations as a secondary instability mechanism. This mode is defined in literature as *type-III*. The frequency of the *type-III* mode has been identified to be one order of magnitude lower than the *type-I-type-II* modes. In addition, the spatial growth rates are significantly lower for this low-frequency mode.

High-frequency fluctuations were experimentally observed by Poll [26] and Kohama et al. [16]. Later, dedicated measurements were performed by Kawakami et al. [14], White and Saric [38], Glauser et al. [11] and Serpieri and Kotsonis [32]. Theoretical studies using secondary linear instability theory were published by Koch et al. [15], Malik et al. [21, 22], Bonfigli and Kloker [3] and Groot et al. [12] while direct numerical simulations were performed by Högberg and Henningson [13] and Wassermann and Kloker [35, 36]. The overall consensus of the aforementioned studies indicates that the convective secondary instability vortices abruptly grow over the strong shear regions caused by the primary waves and eventually lead to laminar-turbulent breakdown within a relatively confined streamwise region. Following this observation, transition prediction approaches, based on the evolution of the secondary instability modes, have been proposed through the years [22, 11].

In comparison to experimental investigations, DNS simulations and theoretical analyses could describe in greater detail these secondary vortices, by inferring their topology and spatio-temporal evolution. The advantage of theoretical/numerical studies over experimental approaches stems from the use of hot-wire anemometry (HWA) and hot-film wall shear measurements as the most used flow diagnostic techniques. These techniques, despite their high spatial and temporal resolution, are limited to single-point and in most cases velocity magnitude and wall shear stresses measurements, thus leading to data which are not correlated in space. Unsteady modes developing in swept wing boundary layers present a multitude of frequencies and wavelengths, pertaining to the aforementioned instabilities. As such, their observation by point measurements like HWA can only be performed in a statistical manner. Full spatio-temporal information can be attained by rigorous knowledge of the phase of the incoming instability.

To overcome this limit of hot-wire based investigations, Kawakami et al. [14] and Chernoray et al. [4] forced the secondary instability (of CFVs in the work of Kawakami et al. and of streamwise roughness-induced vortices in the work of Chernoray et al.) with localized periodic blowing/suction thus locking the phase of the flow structures with the signal of the forcing jet. This approach allowed illuminating measurements, capable of inspecting the spatio-temporal evolution of the travelling modes. Recently, Serpieri and Kotsonis [31] and van Bokhorst and Atkin [34] followed a similar approach as the two aforementioned studies. The work of van Bokhorst and Atkin focussed on the effect of changing the forcing amplitude on the de-

velopment of the secondary modes, whereas Serpieri and Kotsonis presented preliminary results of the current study. A different approach was followed by Glauser et al. [11], making use of multiple sensors (multiple hot-wire probes and multiple hot-films sheets), thus allowing multi-point correlations.

The current study is part of an ongoing effort by the authors to provide experimental description of the complex phenomena describing the evolution and breakdown of laminar swept wing boundary layers. The wind-tunnel facility and model described in this study have been used in a previous study [32], aimed at elucidating the spatial organization of these structures. This was made possible with the deployment of advanced tomographic - PIV [32], yielding spatially resolved measurements of the naturally occurring secondary modes. Nevertheless, due to technical constraints, temporal description was limited. The flow structures were only indirectly related to their pertinent frequencies, measured with HWA, by application of Taylor hypothesis on flow advection. The present study aims at lifting some of these limitations by following a different route, as explained in the following section.

1.2. Present study

In this work, low- and high-frequency modes arising on saturating, roughness-excited CFVs have been conditioned by known predetermined forcing via an Alternating Current Dielectric Barrier Discharge (AC-DBD) plasma actuator specially manufactured for this study and installed on the wing. In contrast to the localized forcing of Kawakami et al. [14] and Chernoray et al. [4], the choice was made for spanwise invariant forcing, enabled by the inherent features of the plasma actuator. Plasma actuators present several attributes rendering them ideal for localized, deterministic actuation of transitional flows [19, 39, 23]. Most pertinent to this study is their ability to work on electrical rather than mechanical time scales, thus able to introduce a wide band of frequencies in the flow. Such band encompasses the relevant frequency range, governing swept boundary-layer instabilities such as the *type-III*, *type-I* and *type-II* modes described in the previous section for the considered flow case [32]. Additionally, through the use of state-of-the-art solid state high voltage amplifiers, the driving signal of the actuator can be deterministically set and measured in order to enable time-stamping and phase-reconstruction of the unsteady structures pertaining to both low- and high-frequency travelling cross-flow instabilities. The capability of adjusting the actuators' control authority by increasing/reducing the voltage amplitude and the inherent directionality of plasma-based forcing enable accurate and deterministic conditioning of flows. As such, apart from their traditional flow control role, plasma actuators become ideal tools for deep fundamental understanding of transitional flows, in an analogous function to the well-known vibrating ribbon. Finally, given the novel plasma actuator fabrication technique, a dedicated experiment was carried out with the aim of evaluating the actuator performance.

The actuator was mounted on a 45 degrees swept wing installed in a low-turbulence facility at TU Delft Aerodynamics, in the same setup as the one used in Serpieri and Kotsonis [32]. The actuator was operated at different voltages and at different forcing frequencies. The deterministic forcing slightly enhanced the amplitude of the secondary instability modes without affecting the primary stationary mode, allowing to narrow their spectral content and to condition their phase. As a consequence, a phase-averaged reconstruction of the hot-wire measurements, based on the actuator signal, was performed. The secondary modes spatio-temporal evolution was captured showing a good agreement with the previous effort of Kawakami et al. [14], Chernoray et al. [4] and with the recent outcomes of the tomo-PIV experiments by Serpieri and Kotsonis [32]. The evolution of the secondary modes at different chord stations and for different actuator positions was investigated. Finally, the effect of the amplitude of the 'carrying' CFV was analyzed and compared to the results of the simulations by Wassermann and Kloker [35] and Choudhari et al. [5] and of the stability computations by Groot et al. [12].

2. Experimental Setup

In this section, the model and the facility used in the current experiments are described along with the flow diagnostics setup. The actuator configuration and performance are also presented in this section. Finally, the coordinate systems and relative velocities notations are introduced.

2.1. Model, wind-tunnel and reference systems

A 45 degrees swept wing of about 1.25m of span (b) and 1.27m of chord in the free-stream direction, when at zero incidence, (c_X) was used. The wing section features a modified version of the NACA 66018 airfoil (see figure 1), named 66018-M3J. The airfoil features small leading edge radius in order to avoid attachment line instability and turbulent contamination from the wind tunnel walls. Flow acceleration until about 70 percent of the chord (at zero incidence) and the convex shape of the wing section suppress Tollmien-Schlichting (TS) waves and Görtler vortices, respectively. More details on the model can be found in Serpieri and Kotsonis [32]. The airfoil used is presented in figure 1. It should be noted that this is the wing section orthogonal to the leading edge.

The wind-tunnel where the experiment was performed is the TU Delft Low Turbulence Tunnel (LTT) facility. This is a closed loop low-turbulence subsonic tunnel with a testing chamber of 1.25m $\times$1.80m of height and width respectively and 2.6m length. The tunnel presents seven anti-turbulence screens and a contraction nozzle with 17:1 cross-section ratio. The turbulence intensity (Tu) measured with a hot-wire sensor and band-pass filtered between 2 and 5000Hz, is $Tu/U_\infty = 0.07\%$ at the free-stream

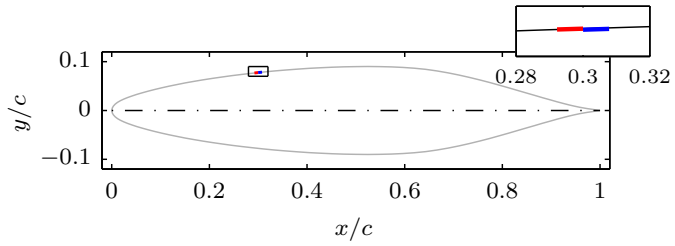

Figure 1: Schematic (to scale) of the airfoil (orthogonal to the wing leading edge) used in the present work with the AC-DBD actuator installed at $x/c = 0.30$. Inset: detailed view of the actuator. Red line: exposed electrode; blue line: covered electrode.

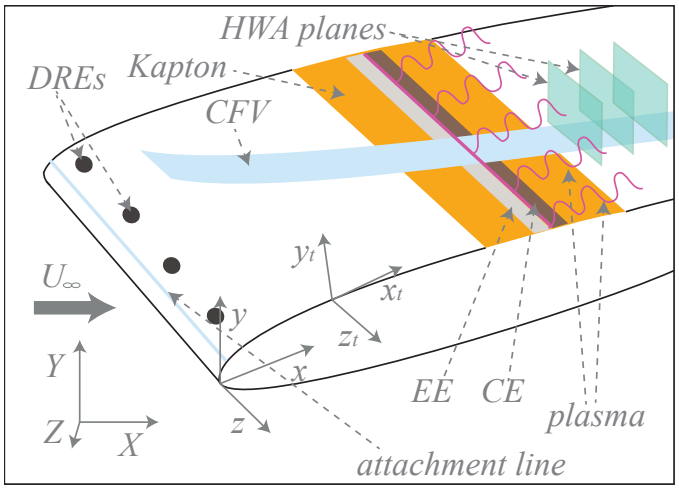

Figure 2: Schematic (not to scale) of the model with leading edge DREs and plasma actuator (EE: exposed electrode; CE: covered electrode and *Kapton* dielectric film). Definition of the reference systems xyz, XYZ and $x_t y_t z_t$. Illustration of the HWA measurement planes, of the stationary CFV, of the attachment line and of the downstream advecting plasma waveforms.

velocity $U_\infty = 24$m/s. This value is low enough to observe stationary cross-flow waves [2]. The wing was set at incidence of $\alpha = 3°$ and the free-stream velocity set at $U_\infty = 25.6$m/s (Reynolds number based on free stream velocity and c_X chord, $Re = \frac{U_\infty c_X}{\nu} = 2.17 \cdot 10^6$). The flow over the wing pressure side (i.e. the geometric side of the wing on which the attachment line is formed) was investigated.

Figure 3 presents the measured pressure coefficient (Cp) distribution at two spanwise stations equally distanced from the model centerline ($\pm 0.3b$) together with the angle of the inviscid streamline w.r.t x (γ). Results indicate satisfactory spanwise invariance for the pressure distribution. Furthermore it is worth to notice that for this flow configuration the measured pressure minimum point is at $x/c = 0.63$ thus avoiding amplification of TS waves, up to this point.

The expedient used by Reibert et al. [27] of fixing the primary (naturally dominant) stationary mode by means of small roughness elements is followed in this study. A sequence of small cylindrical elements (diameter of $d =$

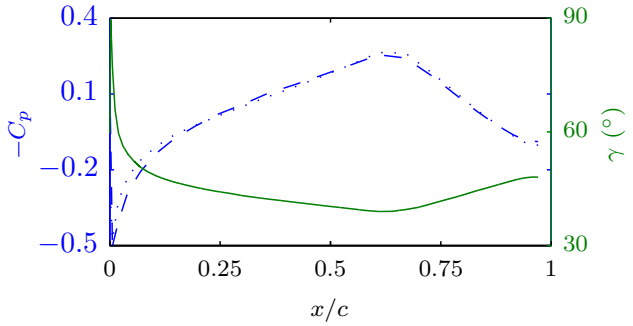

Figure 3: Pressure coefficient (C_p) distribution on the wing pressure side measured by two arrays of 46 pressure taps placed $\pm 0.3b$ (dashed and dotted lines, respectively) from the model centerline at $\alpha = 3°$ and $Re = 2.17 \cdot 10^6$. Angle of the inviscid streamline w.r.t x (γ) (solid line).

2.8mm and average height of $k = 10\mu$m) is installed on the model surface at $x/c = 0.025$, close to the forced mode critical location. The distributed roughness elements (DREs) are installed with a spacing along z of $\lambda_z = 9$mm, matching the wavelength of the dominant stationary wave, as predicted by preliminary linear stability calculations [32]. All the tests presented here are performed under conditions of primary stationary instability critical forcing.

In figure 2, the reference systems used in this study and the respective notations are introduced. The wind-tunnel coordinate system is defined with the upper case letters XYZ and is such that the X and Y axis lie in a horizontal plane, the X being in the chord plane and Y orthogonal to that plane, while the Z is the vertical direction. The velocity components along this coordinate system are indicated with upper case letters UVW. Free-stream quantities are denoted with the subscript ∞. The swept wing reference system is such that its x axis is orthogonal to the wing leading edge, the z parallel to it (both these axes belong to the chord plane) and the y coincides with the Y direction. By rotating the XYZ system of coordinates 45° about the Y axis, one goes to the swept xyz system. The velocity components in this system of coordinates are indicated with the lower case letters uvw. A last coordinate system needs to be introduced here as the local tangential system (the definition of tangential is simplified here as it implies only the surface curvature along the X direction). It is such that its x_t axis is along the surface tangent, the y_t is the wall normal direction and z_t coincides with the Z axis.

2.2. Hot-wire measurements

Hot-wire measurements were performed with a single-wire boundary layer probe (*Dantec Dynamics P15*). A second probe (*Dantec Dynamics P11*) performed simultaneous measurements of the outer inviscid flow. This second probe was mounted about 10cm away from the boundary layer probe along the Y axis at the same $X - Z$

position. This second sensor allowed investigations of the free-stream turbulence levels as well as eventual electromagnetic interference (EMI) from the plasma actuator. Both probes were operated by a *TSI IFA-300* Constant Temperature Anemometer (CTA). Wire calibration was performed in the wind-tunnel itself, far from the model and close to a Pitot-static probe. Flow temperature and atmospheric pressure corrections were applied. The hot-wire was operated at a sampling frequency of $f_s = 40$kHz and low-pass filtered with a cut-off frequency of $f_{co} = 15$kHz before bridge amplification. Time-series of 4 seconds were recorded at every probe position to ensure statistical convergence. A three degrees of freedom automated traverse was installed in the wind-tunnel diffuser. The traverse has a resolution of 2.5μm in all three directions.

The hot-wire scans were performed in $y_t - z$ planes at different chordwise locations corresponding to the primary instability saturation (cf. [32]). Every measured plane consisted of 420 points: 28 scans in the local wall-normal direction y_t times 15 stations in the z direction spaced 0.625mm from each other. The range of the y_t scans was chosen to span from the location where the local mean velocity was 10% of the local outer velocity until the inviscid flow-field. The wires were aligned with the vertical direction such to mainly measure the euclidean sum of velocity components along the axes X and Y: $|V^{HWA}| = (U^2 + V^2)^{\frac{1}{2}}$.

2.3. AC-DBD plasma actuator

The AC-DBD plasma actuator configuration is described in this section. Moreover, given the novel fabrication technique, a dedicated experiment was performed to characterize the actuator mechanical performance.

2.3.1. Configuration

For the needs of this study, actuator-induced roughness is of great importance. To this end, specially developed actuators were employed. These were manufactured using a proprietary silver nanoparticles ink-jet printing technique resulting in electrode thickness of less than 100nm. For comparison, traditional hand-made copper-electrodes actuators typically have electrode thickness of $\approx 60\mu$m. The plasma actuator was placed at two different chordwise positions ($x/c = 0.30, 0.375$) to investigate the effect of the forcing location on transition. The electrodes were aligned with the leading edge-parallel direction (z) and such to induce an air flow along x. The schematic in figure 2 is a representation of the experiment including the wall-mounted actuator. The streamwise length of both exposed (EE) and covered electrode (CE) was 7mm while neither gap nor overlap between the electrodes were present. In figure 1, the exact position ($x/c = 0.30$) and relative dimensions of the AC-DBD actuator w.r.t. the wing section are shown. *Kapton* polyimide film of 50μm thickness was used as dielectric barrier. A second layer of *Kapton* was put between the actuator and the model surface to protect the latter

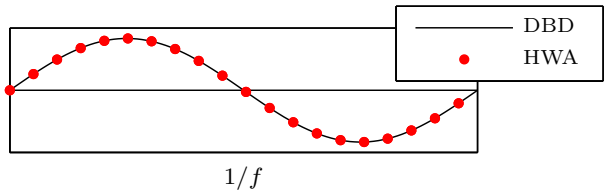

Figure 4: Schematic of the time signal of the AC-DBD actuator voltage and of the hot-wire measurements.

in case of actuator failure (usually translating into spark discharges); as such the total thickness of the actuator was measured to be 125μm (notice that the layer of glue used to mount the actuator also contributes to the total height). Although this value is considerable, it should be noted that the actuator was placed significantly far from the leading edge ($x/c = 0.30, 0.375$), where sensitivity of this flow to two-dimensional roughness is low [29]. Indeed, preliminary flow visualizations (not shown), indicated no adverse effects on the transition location, in a spanwise averaged sense, by the physical presence of the actuator (this point will further addressed in the remainder).

The actuator was powered using a *Trek 20/20C HS* high-speed high-voltage amplifier. Depending on the case, the actuation signal was sinusoidal with amplitudes (E) of 1.2kV and 1.5kV. The high voltage signal frequency (carrier frequency) was chosen such to excite the desired unsteady modes. During the hot-wire measurements, the high-voltage monitor output of the amplifier was concurrently recorded in order to allow the phase-reconstruction procedure. A schematic of the time series of the actuator voltage and of the hot-wire measurements is shown in figure 4. Cases with the actuator operating at two frequencies $f_{DBD} = 0.4$kHz and $f_{DBD} = 4$kHz, proper of the *type-III* and *type-I* instability modes, respectively (cf. [32]), were performed. The hot-wire measurements were performed at acquisition frequency of $f_s = 40$kHz, leading to phase averaged reconstruction of the low-frequency mode ($f_{DBD} = 0.4$kHz) within 100 discrete phases. Each phase average was constructed using 1600 instantaneous measurements. Respectively, the high-frequency mode ($f_{DBD} = 4$kHz) was resolved within 10 discrete phases, using 16000 instantaneous samples per phase.

2.3.2. Performance

A dedicated experiment was performed to asses the performance of the used actuator. High speed particle image velocimetry (PIV) was used to measure the velocity field induced by the actuator in quiescent air. To do so, the setup was enclosed in a box of $1\times0.5\times0.5m^3$. The box was made out of transparent acrylic glass thus allowing optical access. The camera used in this experiment is a *Lavision Imager HS* featuring a sensor of 2016×2016px^2, pixel size of 11μm and 12bits of digital resolution. In order to facilitate higher sampling rates, the camera's active sensor was reduced to 960×440 px^2. The camera was equipped

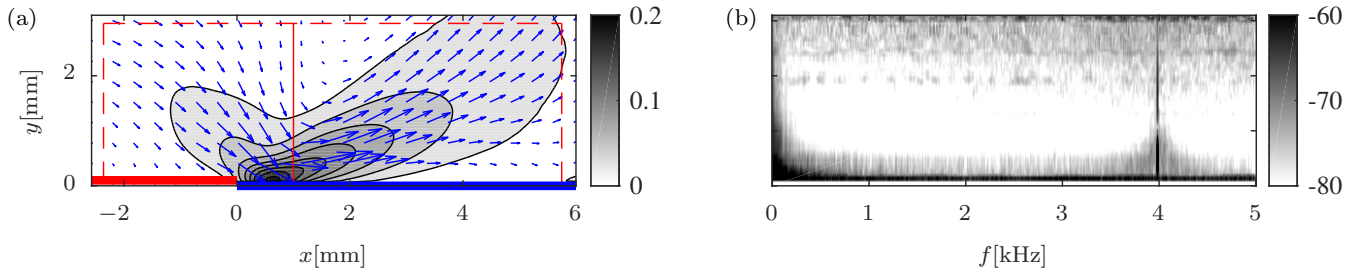

Figure 5: (a) Time-averaged velocity field (one every five vectors shown); shaded: wall-parallel component (m s^{-1}). Red dashed lines: boundaries of the control volume for the evaluation of the exerted thrust. Horizontal thick lines: red EE, blue: CE. (b) Wall-parallel velocity power spectral density (db Hz^{-1}). Velocity sampled along the vertical red solid line of (a).

with a Nikon Nikkor 200mm macro lens and the optical magnification resulted to $M = 1.14$. Paraffin oil particles (*Shell Ondina*), 1μm in average diameter, were generated by a *TSI Atomizer* nozzle. A Nd:YAG high speed *Continuum Mesa PIV* laser (18mJ per pulse) was employed as light source. A 1mm thick light sheet was shaped by means of an opportune set of lenses and aligned with the induced jet, orthogonal to the actuator electrodes. Image acquisition and correlation were performed with *LaVision DAVIS 8.3*. The final vector spacing was approximately 0.053mm in both directions. The system was operated at the acquisition rate of 10kHz in single-frame mode thus the pulse separation between consequent frames was 100μs. Sequences of 25000 images were acquired for each test case for a total measurement time of 2.5s. The high sampling rate and long measurement time ensure to capture both the instantaneous flow evolution as well as the converged statistical fields.

Following Kotsonis [17], the time-averaged velocity field induced by the actuator is used to retrieve the thrust exerted by the actuator. The time averaged wall-parallel field is presented in figure 5(a). The maximum velocity in this direction is 0.19m s^{-1}. When the actuator was mounted on the wing surface (see figures 1 and 2), the induced jet resulted aligned with x_t. The momentum flux, through the boundaries of a control volume large enough to encompass the total body force (see the red dashed lines in figure 5(a)), is computed. For the f_{DBD} = 4kHz - E = 1.2kV case, the actuator thrust, normalised by unit length, in the wall-parallel direction resulted in $T = 2.30\mu$N m_{DBD}^{-1}. From this quantity the momentum coefficient exerted by the actuator follows from equation 1,

$$C_\mu = \frac{T}{\frac{1}{2}\varrho {u_e}^2 \vartheta_u} \tag{1}$$

where ϱ is the air density. Following Serpieri et al. [33], the considered velocity (u_e) and length (ϑ_u) scales are the local (at the actuator position) boundary layer edge velocity and momentum thickness along x for the considered flow-case. These quantities are extracted from numerical solution of the laminar, stationary, incompressible, 2.5-dimensional boundary layer equations (see [30] for formulation and [32] for the results). Therefore at $x/c = 0.30$ ($u_e = 18.36$m s^{-1} and $\vartheta_u = 2.31 \times 10^{-4}$ m), the momentum coefficient attains the value of $C_\mu = 4.82 \times 10^{-5}$ while at $x/c = 0.375$ ($u_e = 19.14$m s^{-1} and $\vartheta_u = 2.53 \times 10^{-4}$ m) it is $C_\mu = 4.06 \times 10^{-5}$ under the assumption that the oncoming flow does not modify the actuator performance [25, 8] and neglecting the mean-flow distortion caused by the developing CF instability. It must be noted that, for fixed voltage and frequency inputs (thus for fixed values of thrust), the relative effect of the forcing at the more downstream position is milder due to the increased momentum loss of the local boundary layer. Moreover, in an accelerating flow, it applies that $u_e(x_1) < u_e(x_2)$ if $x_1 < x_2$. This is the case for the considered flow (see figure 3) thus also contributing to the forcing weakening at more downstream locations.

The values of velocity, thrust and momentum coefficient are relatively low compared to standard applications of AC-DBD plasma actuators [24, 6]. A comparative example is provided by the work of Dörr and Kloker [9], where plasma actuators were used to attenuate non-linear CFVs. Scaling the dimensional force from the study of Dörr and Kloker [9] to the conditions of the present experiment (i.e. $x/c = 0.30$, $u_e = 18.36$m s^{-1} and $\vartheta_u = 2.31 \times 10^{-4}$), an equivalent $C_\mu = 3.31 \cdot 10^{-2}$ is estimated, which is three orders of magnitude larger than the actuator of this study, further confirming the weak nature of the presently used actuators. This is in line with the scope of this experiment which is to condition the unsteady modes without modifying their development or affecting the base-flow. Towards this goal, rather weak jets are required as will be shown in the results section.

When the actuator was supplied with the f_{DBD} = 0.4kHz - E = 1.5kV voltage, the induced jet resulted even weaker thus not allowing to extract the exerted thrust with acceptable accuracy despite the slightly augmented voltage amplitude to compensate the frequency response of the actuator [24, 6]. A consequence of the reduced carrier frequency is that the actuator lifetime can be significantly longer (several tens of hours of operation), compared to high-frequency forcing. Vice-versa operation at high frequencies causes dielectric failure after a few hours of operation. The limited lifetime of the considered actuator at high frequency necessitated a restricted testing matrix for

high-frequency forcing in this study as it will be shown in section 3.

Capitalizing on the very high frame rate of the PIV experiment, spectral information of the induced velocity field is also accessible. The Power Spectral Density (PSD), computed following Welch's method [37], with final frequency resolution $\delta_f = 10$Hz, of the wall-parallel velocity signal sampled along the solid line of figure 5(a) is shown in figure 5(b). It appears that most of the spectral energy occurs at the carrying voltage frequency as reported in previous studies on standard actuators [6] thus confirming the capability of the considered actuator in forcing the chosen narrow-band fluctuations. However, increased spectral energy at relatively low frequencies ($0 < f < 0.2$ kHz) is also evident in figure 5(b). At this point it cannot be concluded whether this low-frequency component is an artefact of quiescent-conditions testing (i.e. recirculation in the box, drafts etc.) or an inherent plasma oscillation.

Finally, a note must be made regarding the use of HWA in close proximity to plasma actuators. Hot-wires are electrically balanced devices, relying on minute variations of voltage signals, thus sensitive to electromagnetic noise. Previous studies have shown pronounced levels of electromagnetic interference affecting the hot-wire when in the vicinity of operating plasma actuators [20, 17]. Typically EMI would appear as a narrow peak in the measured signal at the plasma carrier frequency. In the present study, the effect of EMI was identified by utilizing the second hot-wire probe positioned in the inviscid flow and measuring concurrently to the boundary layer probe. As it will be shown in the results section, EMI effects were detected by the inviscid-flow hot-wire, albeit several orders of magnitude less energetic than the physical velocity fluctuations pertaining to boundary-layer instabilities, detected by the boundary layer probe (see figure 7). As such, the effect of EMI on the statistical and phase-reconstructed flow fields was confirmed to be negligible. The relatively low levels of EMI can be attributed to the large distance between the plasma actuator and the hot-wires (minimum distance was approximately 120 mm) and the relatively low amplitude of high voltage.

3. Investigated cases

The plasma actuator was operated at two different voltages in order to reconstruct the spatio-temporal characteristics of the two developing instability modes of *type-I* (in the 4000Hz band) and *type-III* (in the 400Hz band) [32]. These fluctuations were weakly amplified by the actuation and their respective phase was locked to the actuator signal as it will be shown in section 4.4.

Measurements were performed at four different chordwise stations ($x/c = 0.40, 0.425, 0.45, 0.475$) for both the unforced and the low-frequency forcing cases. Given the reduced lifetime of the dielectric *Kapton* sheet when the actuator was operated at the higher frequency and the long measurement time necessitated by HWA measurements (about 40 minutes were needed per each measured plane), only the plane at $x/c = 0.45$ was measured for the 4kHz forcing case. The three investigated cases are summarized in table 1.

4. Results and discussion

The effect of periodic forcing on the statistical flow fields is inspected in the following section. The spectral content is analysed by means of single-point spectra and band-pass filtered fields followed by the investigation of the spatio-temporal evolution of the unsteady modes. Finally, the effect of the amplitude of the 'carrying' stationary vortex and of the actuator position is presented.

4.1. Statistical analysis

As described in the experimental setup, the hot-wire probe was aligned such to measure mainly the euclidean sum of the U and V velocity components. Time averaged (denoted with the overbar symbol) velocity fields non-dimensionalised with the local external velocity ($|\bar{V}_e^{HWA}|$) and pertaining to the three investigated cases are presented in figure 6. For all cases, the characteristic structure pertaining to the fully developed cross-flow vortex is evident at the chordwise location of $x/c = 0.45$. Previous extended investigations by the authors [32] showed that, at this station, the primary stationary vortices are undergoing amplitude saturation. Based on the same study and previous works [7, 22, 35, 38], amplitude saturation of the primary CF mode is usually accompanied by rapid growth of secondary high-frequency instabilities. The stationary CF vortices have very weak in-plane velocity components compared to the component along the vortices axes [35, 32]. Nonetheless, the displacement of high momentum fluid in low-momentum regions (and vice-versa), consequence of these vortices, has a dramatic impact in the organization of the boundary layer. The contours presented in figure 6 clearly show this effect. Furthermore, it can be concluded that the unsteady plasma forcing at both the lower and higher frequency does not produce any considerable effect on the morphology of the stationary vortices.

Inspection of the velocity fluctuation fields, provided in figure 6, for the three flow cases shows pronounced fluctuations levels. These are mainly occurring in two regions of the boundary layer corresponding to the inner and the outer upwelling flow regions of the primary vortex. Malik et al. [22] showed that these regions correspond to the locations of large positive and negative values of the spanwise velocity gradient respectively. Previous research (e.g. [13, 22, 14, 35, 38]) showed that the outer side of the cross-flow vortices is occupied by high-frequency fluctuations, defined as *type-I* mode, of Kelvin-Helmholtz nature (cf. Bonfigli and Kloker [3]). The inner region of the primary vortices is instead interested by low-frequency fluctuations,

Table 1: Investigated cases

Instability mode	f_{DBD} [kHz]	E [kV]	HWA planes: x/c			
natural flow	-	-	0.40	0.425	0.45	0.475
type-III	0.4	1.5	0.40	0.425	0.45	0.475
type-I	4.0	1.2	-	-	0.45	-

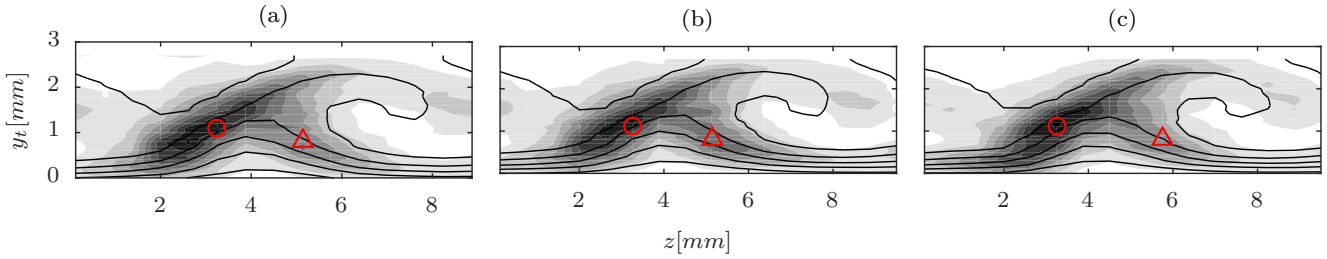

Figure 6: Time averaged velocity fields (solid lines: 7 levels, from 0 to $|\bar{V}_e^{HWA}|$) and velocity fluctuation fields (shaded: 10 levels, from 0 to $0.1|\bar{V}_e^{HWA}|$) at $x/c = 0.45$. AC-DBD actuator installed at $x/c = 0.30$: (a) non-operative; (b) $f_{DBD} = 0.4$kHz - $E = 1.5$kV; (c) $f_{DBD} = 4$kHz - $E = 1.2$kV. The red markers indicate locations of spectral analysis presented in figure 7.

related to the *type-III* mode, which arise from the interaction between the stationary and the travelling cross-flow waves, with the latter featuring the reported lower frequencies and growth rates [10, 13, 22, 14, 35, 3].

Upstream plasma forcing at $x/c = 0.3$ results in mild changes in the distribution of dominant fluctuations within the stationary CFV flow-field. By operating the actuator at the frequency of $f_{DBD} = 0.4$kHz, the *type-III* mode is enhanced. This is confirmed by the contour of figure 6(b), where the fluctuations in the inner 'leg' of the stationary vortex are slightly increased. When instead the unsteady forcing is applied at $f_{DBD} = 4$kHz, the *type-I* fluctuations are stimulated. The contour of figure 6(c) indicates a slight increase of fluctuations associated with the left leg of the vortex.

The apparent invariance of the statistical flow-fields to actuation confirms the initial premise of utilization of the AC-DBD actuator as a forcing agent with minimal effect on the base flow. This was achieved using rather weak high voltage amplitudes as well as placing the actuator in the fully developed primary instability field but considerably upstream of the secondary modes onset (i.e. marginal stability branch-I). Further discussion on the effect of the actuator position is provided in section 4.6.

4.2. Spectral analysis

It is instructive to inspect the effect of the unsteady forcing of *type-III* and *type-I* instability modes in the spectral domain. To this goal, the hot-wire velocity signal was sampled at locations of fluctuations maxima described in the previous section and corresponding to the marker positions in the flow-field of figure 6. Averaged periodogram PSD were computed [37]. The spectra feature a frequency resolution of $\delta_f = 10$Hz. The presented spectra are normalised based on Parseval's theorem as shown in equation 2,

$$PSD^*_\gamma \cdot \delta_f = (PSD_\gamma \cdot \delta_f) \frac{\sqrt{\frac{1}{ES-1}\Sigma_t(\gamma')^2}}{\Sigma_f(PSD_\gamma \cdot \delta_f)} \qquad (2)$$

where γ is the spectra variable and ES the temporal ensemble size. The sums are performed w.r.t the subscript quantity (i.e. time (t) at the numerator and frequency (f) at the denominator).

The spectra of the fluctuations maximum in the outer upwelling air region are presented in figure 7(a) for the three investigated flows. The spectra show that at the higher frequencies, when the 4kHz forcing is applied, the broadband energy between 3 and 7.5kHz (related to the *type-I* mode) attains to lower levels compared to the unforced and low-frequency forcing cases. The spectra of these two last cases are practically overlapping on each other throughout the resolved band. Nevertheless, the energy at 4kHz is considerably increased thus showing the possibility of conditioning the frequency of the secondary modes through external monochromatic forcing. Furthermore, the spectrum of the high-frequency forcing shows enhanced energy levels throughout the band suggesting a contamination of fluctuations, due to actuation. The low-frequency forcing shows discrete peaks stemming beyond the unforced case spectrum at the forcing frequency and at the first two harmonics (400, 800 and 1200Hz).

The spectra sampled at the location of maximum fluctuation in the inner CFV leg are shown in figure 7(c). As for the previously discussed spectra, the 4kHz forcing has stronger effects on the full spectrum fluctuations. The 400Hz forcing shows higher peaks at the forcing frequency and at the first five harmonics (untill 2kHz). All spectra feature a broadband hump centred at $f = 0.4$kHz. This hump is related to the *type-III* mode [32]. Moreover, the fluctuations comprised in the band 500Hz$\leq f \leq$2kHz

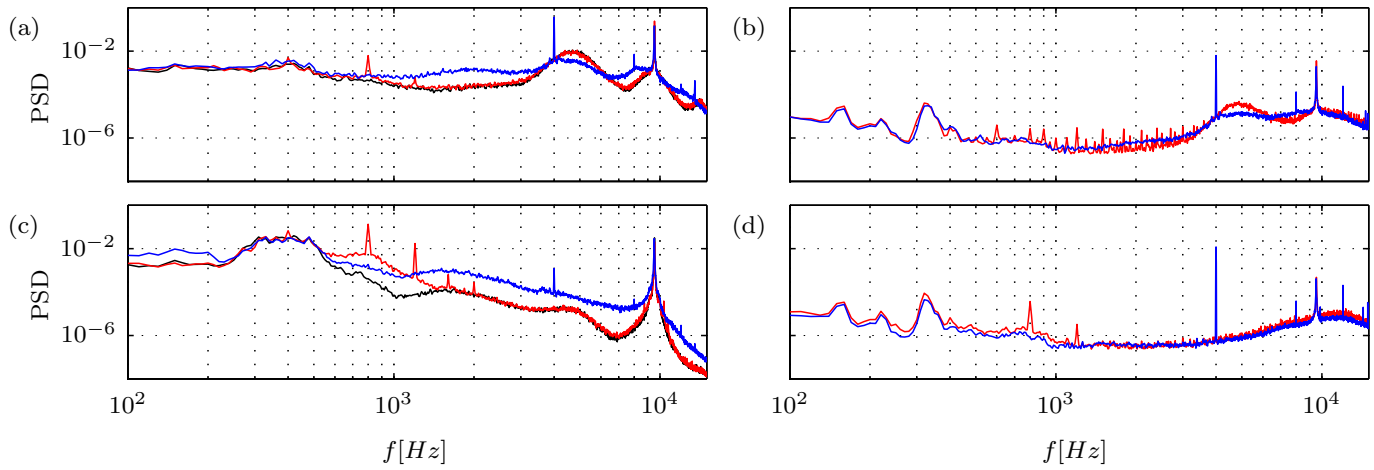

Figure 7: Normalised power spectral densities of the velocity fluctuations (see equation 2) at $x/c = 0.45$. Velocity sampled at the location of local maximum of fluctuations in (a) the outer upwelling air region (denoted by ◯ in figure 6) and (c) the inner upwelling air region (denoted by △ in figure 6). Velocity sampled in the outer inviscid flow (b) simultaneously to (a) and (c) simultaneously to (d). Black lines: unforced flow; red solid lines: $f_{DBD} = 0.4$kHz; blue solid lines: $f_{DBD} = 4$kHz.

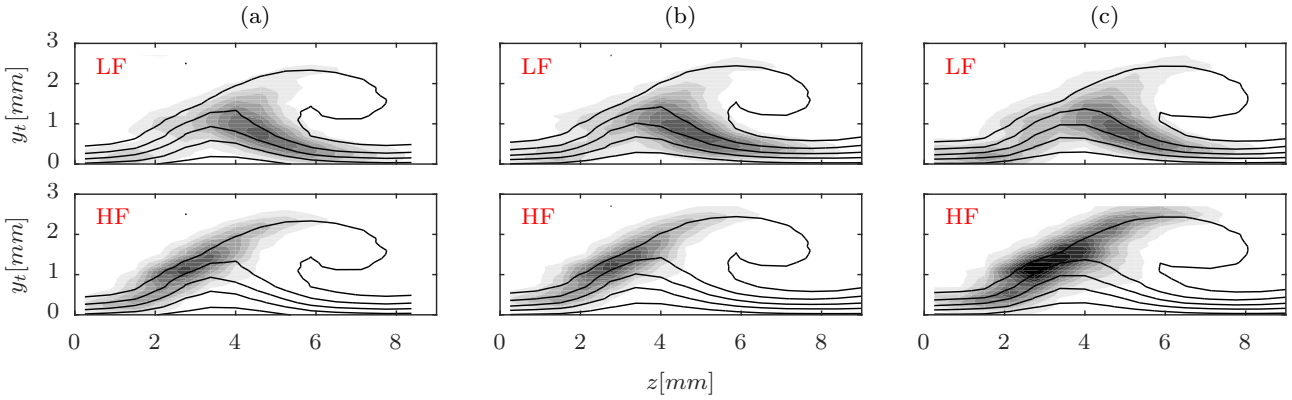

Figure 8: Contours of the band-pass filtered (top: LF; bottom: HF) fluctuations (shaded, 10 levels from 0 to $0.05 \cdot |\bar{V}_e^{HWA}|$) at $x/c = 0.45$. AC-DBD actuator installed at $x/c = 0.30$: (a) non-operative; (b) $f_{DBD} = 0.4$kHz - $E = 1.5$kV; (c) $f_{DBD} = 4$kHz - $E = 1.2$kV. Black line contours denote time averaged velocity.

are significantly increased, even beyond the high-frequency forcing spectrum, by the 400Hz forcing.

The spectra of the second hot-wire placed outside the boundary layer (about 10cm from the boundary layer probe) at the same $X - Z$ position are plotted in figures 7(b) and (d). They show different discrete spikes that are to be related to electro-magnetic interference (EMI). Despite the undesired occurrence of these spikes their overall energy is several orders of magnitude lower than the pertinent frequencies in the boundary layer, suggesting negligible influence of EMI on the measurements. The high-frequency hump of the second wire signal is instead an artefact of the CTA hardware [28].

To further evaluate the effect of the applied forcing on the boundary layer, the velocity fluctuations were band-pass filtered in the relevant frequency bands by means of fourth order Butterworth digital filters [32]. The two inspected bands covered frequencies between 350Hz and 550Hz (low-frequency (LF) band) and between 3.5kHz and 4.5kHz (high-frequency (HF) band) respectively. The analysis was performed for the three flow cases investigated so far and is presented in figure 8. It is evident that the unsteady modes are strictly confined in the described zones of the boundary layer. Forcing at the high frequency has major effects, given that the spectral peak of the *type-I* mode is much higher than the respective low-frequency band under low-frequency actuation. The analysis of the spectra and band-pass filtered fields allows to conclude that the chosen operating voltages for the two forced frequencies (summarized in table 1) are enough to enhance the desired instability modes, without strongly affecting the overall evolution of the boundary layer, or the transition process.

To quantify the field amplitudes of the primary and secondary instability mechanisms, opportune metrics can be introduced. Following White and Saric[38] and Serpieri and Kotsonis[32], the primary stationary instability amplitude is retrieved from the wall-normal integral of the

Table 2: Stationary (A_I) and unsteady full spectrum (A_{II}^{tot}), band-pass filtered (A_{II}^{LF}: low-frequency band, A_{II}^{HF}: high-frequency band) and phase-reconstructed (A_{II}^{PR}) disturbances amplitudes from equations 3 and 4 evaluated at $x/c = 0.45$.

forcing	A_I	A_{II}^{tot}	A_{II}^{LF}	A_{II}^{HF}	A_{II}^{PR}
none	0.119	0.0302	0.0058	0.0048	-
0.4 [kHz] - 1.5 [kV]	0.1181	0.0329	0.0069	0.0050	0.0042
4.0 [kHz] - 1.2 [kV]	0.1175	0.0352	0.0074	0.0091	0.0064

mode shape profiles (i.e. the spanwise standard deviation of the time-averaged velocity profiles). The mathematical expression of this quantity is in reported in equation 3,

$$A_I(x) = \frac{1}{y_t^m} \int_0^{y_t^m} \left\{ \frac{|\bar{V}^{HWA}(x)|}{|\bar{V}_e^{HWA}(x)|} \right\}_z dy_t \tag{3}$$

where the brackets define the standard deviation operator w.r.t. the subscript quantity (z). Similarly, the amplitude of the total and of the two band-pass filtered fluctuations fields is obtained by integrating, over the measured plane, the temporal standard deviation fields of the considered frequency band. The formulation of this quantity is reported in equation 4,

$$A_{II}(x) = \frac{1}{y_t^m} \frac{1}{z^m} \int_{f_1}^{f_2} \int_0^{y_t^m} \int_0^{z^m} \left\{ \frac{|V^{HWA'}(x)|}{|\bar{V}_e^{HWA}(x)|} \right\}_t dz dy_t df \tag{4}$$

where $z^m = \lambda_f = 9$mm.

The quantity A_{II} is evaluated for the total spectrum (A_{II}^{tot}, with $f_1 = 0$Hz and $f_2 = f_s/2$) and for the low (A_{II}^{LF}, with $f_1 = 350$Hz and $f_2 = 550$Hz) and high (A_{II}^{HF}, with $f_1 = 3.5$kHz and $f_2 = 4.5$kHz) frequency bands. Therefore the fluctuation fields shown in figure 6 and 8 are the considered integrands of equation 4. Finally, A_{II}^{PR} is the fluctuations amplitude of the phase-reconstructed (PR) mode with $f_1 = f_{DBD} - \delta_f$ and $f_2 = f_{DBD} + \delta_f$ (note that this is true under the assumption that, through phase averaging, only the fluctuations pertaining to the monochromatic reconstructed mode are considered). The results are summarized in table 2. The unforced stationary vortex, at the measurement location, reached the amplitude of $A_I = 0.119$. Comparing this value with the one reported at the same chordwise station and flow conditions by Serpieri and Kotsonis [32] (c.f. figure 11a) where no actuators were mounted on the wing ($A_I = 0.113$), shows that the steps caused by the layer of dielectric have no effect on the developing stationary cross-flow instability.

When the actuator is operated, the amplitude of the CFV is slightly decreased by the enhanced fluctuations. Moreover, forcing at both the considered frequencies causes an increase of the fluctuations amplitude in both the forced band and in the full spectrum amplitude with the higher frequency forcing showing the largest effects (as seen in figure 8).

4.3. Spatial evolution

In this section, the effect of the forcing on the chordwise development of the stationary and unsteady fields is investigated. For this purpose, the same cross-flow vortex analysed so far is traced along the x direction, considering that the CFVs are roughly aligned with the local flow ([32] and figure 3). Measurements were therefore performed at three more chordwise positions: $x/c = 0.40, 0.425, 0.475$. The hot-wire scans have the same spanwise resolution (0.625mm) as for station $x/c = 0.45$. However, the wall-normal scans are slightly adjusted to compensate the different wall-normal extent of the boundary layer while still encompassing 28 points per wall-normal profile. For this analysis both the unforced boundary layer as well as the $f_{DBD} = 0.4$kHz - $E = 1.5$kV case were considered.

In figure 9, the fluctuation amplitudes are plotted versus the measured locations together with their chordwise gradient. It appears that, for the most upstream station ($x/c = 0.40$), both the steady modes and the fluctuation amplitudes are not strongly affected by the actuation. However, the amplitude gradients (representative of local growth rates) of both stationary and unsteady fields are initially larger for the forced cases. Therefore, at $x/c = 0.45$, larger amplitudes in all the three considered bands are observed, as discussed before. Similar effects occur when the actuator is operated at the higher frequency. The stationary mode amplitude at $x/c = 0.45$ is almost the same for all the three cases, however the higher fluctuations for the forced field lead to the reduced A_I amplitude at the most downstream station. This indicates a more advanced transitional state with enhanced diffusion of the steady structures.

4.4. Spatio-temporal organisation

It becomes evident from the spectral analysis (figure 7) and band-pass filtered fluctuation fields (figure 8), that actuation at the selected frequencies results in the forcing of the respective instability modes. Due to the deterministic conditioning of both forcing signal and acquisition sequence, it can be expected that the triggered modes will be phase conditioned. This allows the reconstruction of the coherent spatial structures pertaining to these modes (the details were discussed in section 2.3), thus enabling phase-resolved measurements using a point measurement technique (HWA) [14, 4].

Phase-averaged velocity fluctuation fields (mean flow subtracted) in the $y_t - Z$ plane are presented in figure 10 for the low-frequency forcing and in figure 11 for the high-frequency forcing (10 equally spaced phases for both the forced modes). For both the modes, it appears that,

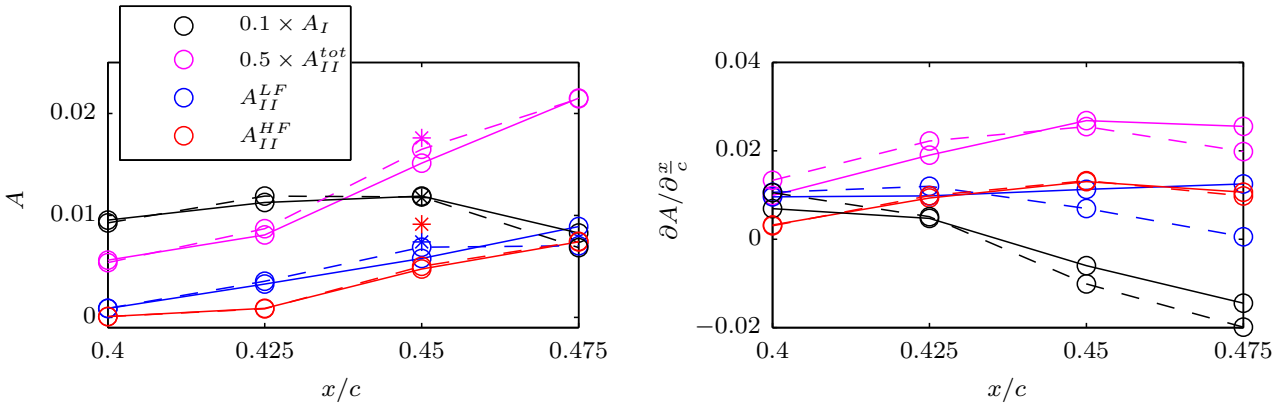

Figure 9: Chordwise evolution of stationary modes and fluctuations amplitudes (see equations 3 and 4) and related chordwise gradients. Solid lines: unforced flow; dashed lines: actuator operated at $f_{DBD} = 0.4$kHz - $E = 1.5$kV; symbol $*$: actuator operated at $f_{DBD} = 4$kHz - $E = 1.51.2$kV.

increasing phase (i.e. increasing time), the fluctuations maxima tend to move towards the wall. More specifically, the structures pertaining to $f_{DBD} = 0.4$kHz move towards the right side of the stationary vortex (increasing z and decreasing y_t), while the structures pertaining to $f_{DBD} = 4$kHz displace towards the outer side on the left of the primary vortices (decreasing z and y_t) [14]. In order to better facilitate the topological description of the phase-resolved fluctuating structures, use of a 'pseudo-spatial' representation is made. This is achieved by representing time (i.e. subsequent phases) as the third dimension, where the individual slices in the $y_t - z$ plane are the measured phase averages. This approach is followed in figures 12a and 12b for the low- and the high-forcing frequencies, respectively. The plotted structures are captured at a fixed streamwise position, hence, to represent their 'pseudo-spatial' evolution, they are presented along the decreasing time direction (cf. [14]). This procedure can be mathematically expressed by the equation of a downstream propagating wave at a fixed spatial station x_0: $A(x_0, t) = sin(\alpha_x x_0 - \omega t)$, where α_x is the wavenumber and ω the angular frequency.

Such representation is to be considered only for facilitating visualization and not as a quantitative description of the spatial evolution of the mode. In the latter case, several limitations occur. The spatial amplification of the instability modes cannot be assessed by single-plane measurements. To properly capture the spatial evolution, full volumetric scans are required (see Chernoray et al. [4]). Alternatively, the true spatial evolution could be retrieved from the advection speed of the travelling waves. Serpieri and Kotsonis [32] estimated the convecting velocity by matching it with the local time-averaged boundary layer velocity. This approach is corroborated by the consideration that these structures are generated by inviscid instability mechanisms and hence are passively advected by the local flow (cf. Malik et al. [22] and Bonfigli and Kloker [3]). This would allow to extrapolate the spatial shape and evolution of the unsteady structures. Despite these considerations, the authors believe that the rigorousness of this approach, applied to the current experiment, would suffer for several reasons. The estimation of the local boundary layer velocity from the time-averaged fields is considered as a blunt approximation. In fact, the hot-wire measurements were performed in planes aligned with $y_t - z$ hence not orthogonal to the primary CF vortices (direction of advection). Furthermore, the hot-wire measured the velocity magnitude of the U and V velocity components and not the velocity component along the stationary waves. Only the latter gives a correct estimation of the actual advecting velocity [32]. Due to these considerations, the 'pseudo-spatial' (i.e. decreasing time) representation was chosen.

Despite these limitations, figures 12a and 12b are considered an illustrative visualization. For a direct comparison between the two modes, the presented time-evolution refers to the full period of the lower forced frequency ($T = 1/min(f_{DBD}) = 2.5\mu$s). Hence the structures pertaining to $f_{DBD} = 4$kHz have been replicated over ten periods. The low-frequency structures appear as a sequence of positive and negative velocity regions in the inner upwelling air region of the stationary CF wave. In the 'pseudo-spatial' representation they appear oriented with a shallow angle pointing towards the inner part of the stationary waves and slightly slanted towards the upper region of the boundary layer.

The high-frequency fluctuations pertaining to the *type-I* mode have a drastically different shape, compared to *type-III* structures. In figure 12b they appear as a more narrow sequence of high- and low-velocity structures riding on the outer side of the stationary vortices. The 'pseudo-spatial' plot shows that these waves appear significantly inclined with respect to the stationary vortices. It has to be stressed again that the third axis of figure 12b is in the direction of decreasing time. Hence the plotted structures, not accounting for the effective advecting velocity, do not accurately describe the three-dimensional shape of the instabilities but only give an indication of it. It can

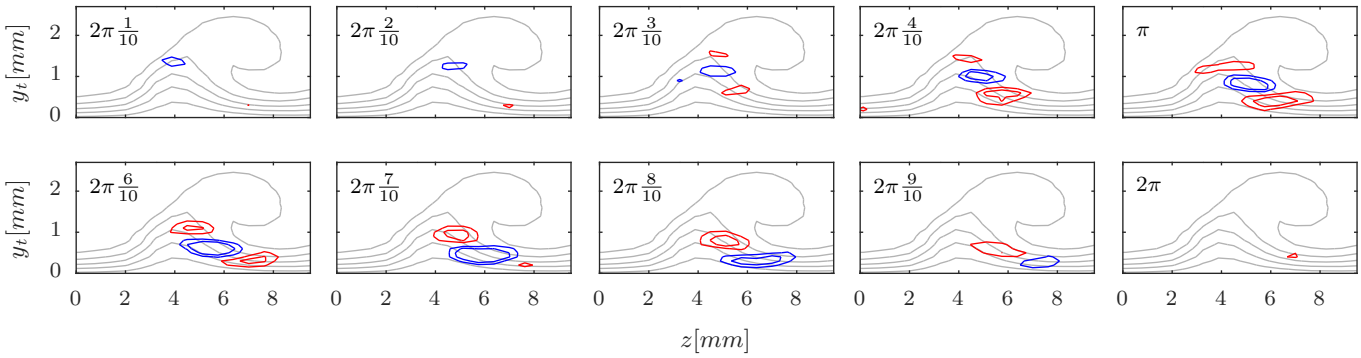

Figure 10: Phase reconstructed velocity fluctuation fields at $x/c = 0.45$: ten equally spaced (see the upper left corner label) phases (5 levels, red lines between $-0.03|\bar{V}_e^{HWA}|$ and $-0.003|\bar{V}_e^{HWA}|$; blue lines between $0.003|\bar{V}_e^{HWA}|$ and $0.03|\bar{V}_e^{HWA}|$) superimposed on contours of time-averaged velocity (grey lines: 6 levels, from 0 to $|\bar{V}_e^{HWA}|$). AC-DBD actuator installed at $x/c = 0.30$ and operated at $f_{DBD} = 0.4$kHz - $E = 1.5$kV.

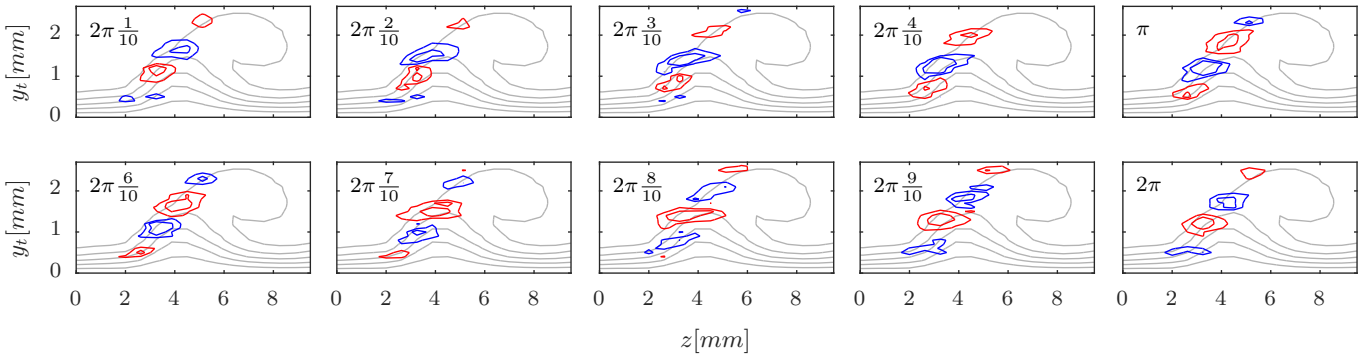

Figure 11: Same caption as figure 10 (5 levels, red lines between $-0.04|\bar{V}_e^{HWA}|$ and $-0.004|\bar{V}_e^{HWA}|$; blue lines between $0.004|\bar{V}_e^{HWA}|$ and $0.04|\bar{V}_e^{HWA}|$) superimposed on contours of time-averaged velocity (grey lines: 6 levels, from 0 to $|\bar{V}_e^{HWA}|$). AC-DBD actuator installed at $x/c = 0.30$ and operated at $f_{DBD} = 4$kHz - $E = 1.2$kV.

be commented that the structures span along the wall-normal direction through almost the entire boundary layer extent. As such, the local flow velocity, by which they are advected downstream, varies considerably thus leading to a more pronounced helicoidal shape w.r.t. the plotted figure [35, 4, 3, 32]. The 'pseudo-spatial' representation of the two modes closely resembles the structures presented by Serpieri and Kotsonis[32] from the Proper Orthogonal Decomposition (POD) analysis of the instantaneous tomo-PIV fields (compare figure 26 and 28 of [32] with figures 12a and 12b in the present study). The convincing qualitative agreement offers a validation of the Taylor hypothesis based estimation of the structures frequencies followed by Serpieri and Kotsonis [32].

In both phase-reconstructed fields of figures 10 and 12a and 11 - 12b, the amplitude of the high- and low-velocity fluctuations appears not constant throughout the reconstructed period. To better visualize this effect, the integral over the measured plane of the square power of the fields presented in figures 10 and 11 is computed per each phase. The expression of this amplitude, referred to as A_Φ^{PR}, is presented in equation 5,

$$A_\Phi^{PR}(x,\Phi) = \frac{1}{y_t^m}\frac{1}{z^m}\int_0^{y_t^m}\int_0^{z^m}\left(\frac{|V_{PR}^{HWA}(x,\Phi)|}{|\bar{V}_e^{HWA}(x)|}\right)^2 dzdy_t \tag{5}$$

where $|V_{PR}^{HWA}|$ is the phase-reconstructed velocity field at each phase. The evolution along the period of the reconstructed fluctuations is presented in figure 13 for both the low- and high-frequency fields. Both these amplitudes show an oscillation within the respective period. This effect can be attributed to the characteristics of the chosen actuator. AC-DBD plasma actuators are known to yield both a DC and an AC body force caused by the different momentum of the species accelerated within the actuation cycle [24, 6, 18]. Therefore, the modulation of the fluctuations energy along the period can be considered as an effect of the actuator.

4.5. Effect of stationary CFVs amplitude

The effect of the 'carrying' primary stationary CFV on the unsteady field is investigated in this section. For this purpose, the experimental setup is partially modified.

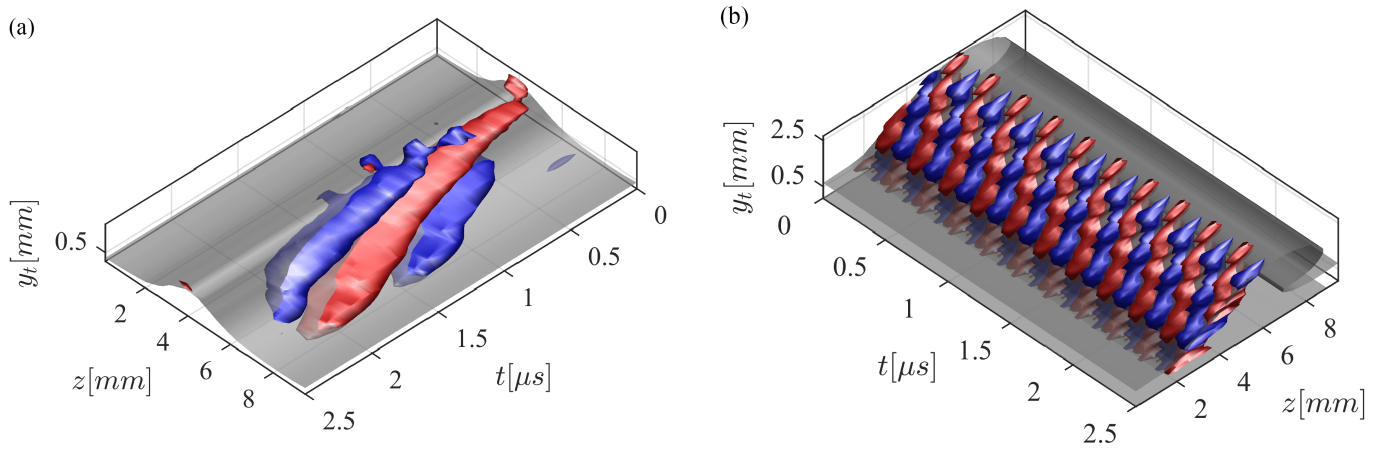

Figure 12: 'Pseudo-spatial' representation of the phase-reconstructed fields (red and blue iso-surfaces at $\pm 0.02|\bar{V}_e^{HWA}|$) (a) of figure 10 ($f_{DBD} = 0.4$kHz (one period), view from upstream and larger z) and iso-surface of the time-averaged velocity (grey iso-surface at $0.6|\bar{V}_e^{HWA}|$); and (b) of figure 11 ($f_{DBD} = 4$kHz (ten periods), view from upstream and smaller z) and iso-surface of the time-averaged velocity (grey iso-surface at $0.9|\bar{V}_e^{HWA}|$).

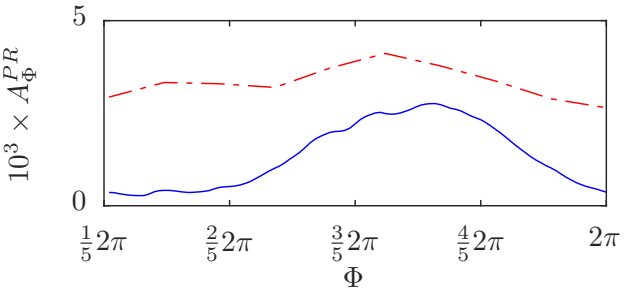

Figure 13: Amplitude of the reconstructed velocity fluctuation fields (evaluated according to equation 5) along one period. Solid blue line: fields of figure 10; dotted-dashed red line: fields of figure 11.

While the flow conditions and measurement approach are the same as described in section 2, the leading edge forcing of the stationary CFV is slightly modified. The micrometric roughness element triggering the stationary vortex was applied with higher force on the model surface, thus slightly reducing the effective protuberance height (see the difference between the two CFVs in figure 16 of [32]) and therefore the initial amplitude of the stationary wave. While measuring the element height (using a mechanic profilometer) could not help to retrieve an accurate estimate (measured uncertainty about $\pm 1\mu$m), the measured velocity field can be used, by means of equation 3, to extract the effect, at the scan location, on the developing stationary wave. The stationary amplitude for the weaker CFV considered in this section at $x/c = 0.45$ is $A_I = 0.1078$. This value is about ten percent less than the modal amplitude of the stronger vortex at the same position analysed in the previous sections (cf. table 2).

Measurements were carried out for the same actuator operating conditions and at the same chordwise positions reported in table 1. The chordwise evolution of the stationary and fluctuation amplitudes and their chordwise gradients are shown in figure 14. Despite the reduced amplitude at the most upstream station ($x/c = 0.40$), the stationary mode attains to comparable saturation amplitudes to what is reported in table 2. Furthermore, also for this flow-case, saturation takes place in the proximity of $x/c = 0.45$ (within the chordwise resolution of the current experiment). Stronger differences between the higher amplitude CFV (figure 9) and the reduced amplitude CFV (figure 14) relate to the fluctuations fields. The unforced weaker CFV features a full-spectrum amplitude of $A_{II}^{tot} = 0.0175$ compared to $A_{II}^{tot} = 0.03024$ for the stronger vortex at $x/c = 0.45$. In a similar way, the band-pass filtered fields are significantly reduced.

The phase reconstruction procedure, described in section 4.4, is performed, at $x/c = 0.45$, for the unsteady field of the weaker CFV. The results are plotted in figures 15 for the reconstructed low-frequency mode. The presented fields attain lower values compared to the respective modes along the stronger CFV presented in section 4.4. The reconstructed fields for the high-frequency forcing yield very weak results and are not shown. The lower frequency correlated band amplitude is $A_{II}^{PR} = 0.0025$ while the high-frequency mode yields $A_{II}^{PR} = 0.0029$ thus about half compared to the values of the stronger wave (see table 2).

Malik et al.[22] analysing the terms of the secondary modes energy equation (namely the Reynolds-Orr equation), showed that the amplification of the *type-I* mode scales with the intensity of the stationary field velocity gradient along the spanwise direction while the *type-II* mode amplification is a function of the wall-normal shears. Because of this relationship, they introduced the alternative

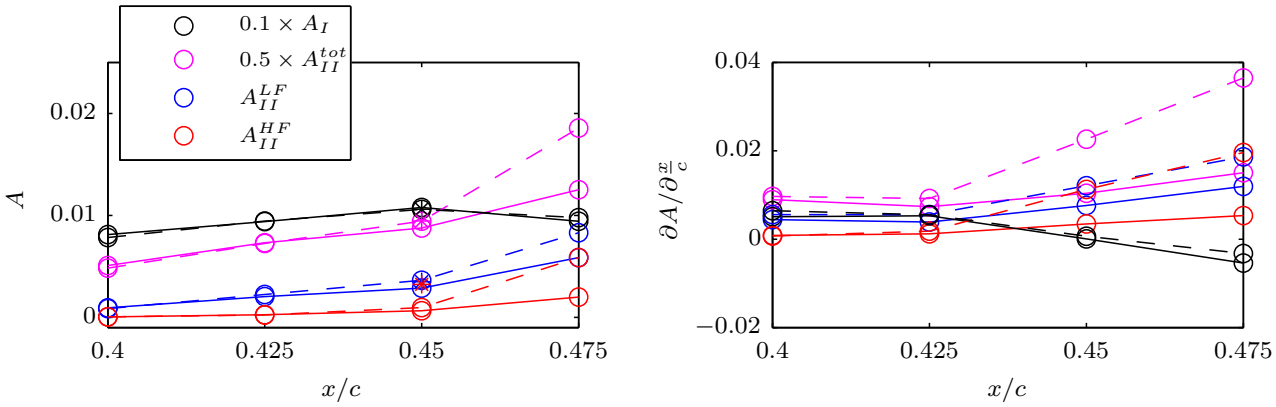

Figure 14: Same caption as figure 9. Reduced amplitude CFV.

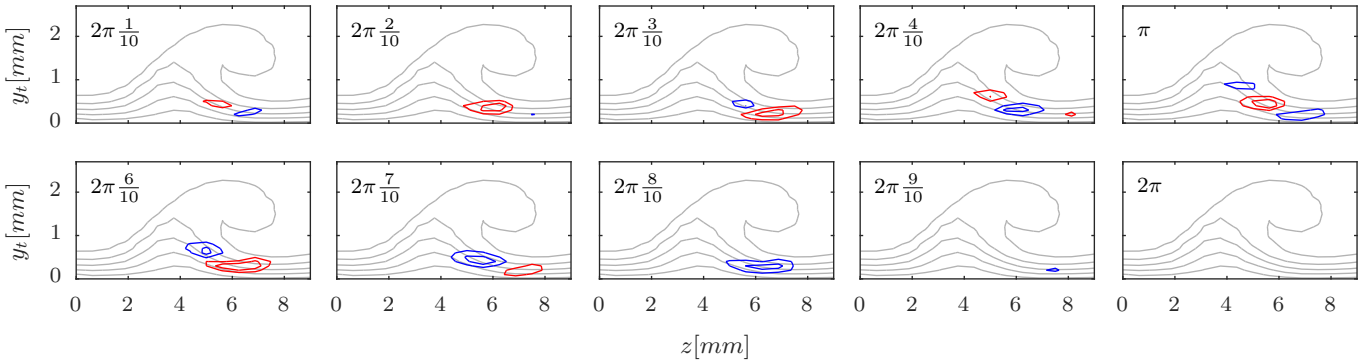

Figure 15: Same caption as figure 10. Reduced amplitude CFV.

nomenclature of *mode-z* and *mode-y* for the two modes. Groot et al.[12] followed a similar approach (linear secondary stability theory) but making use of the experimental flow-field measured with tomographic PIV by Serpieri and Kotsonis[32] as base-flow. The experimental flow-field encompassed both the stronger and the weaker CFVs investigated in this study. One of the results shown by Groot et al.[12] is that the secondary *type-I* and *type-II* instability modes of the weaker wave are marginally stable while those of the stronger vortex are both unstable (and for a broad band of wavenumbers/frequencies). The energy terms analysis revealed that, for both the modes, the Reynolds stresses related to the spanwise shears were reduced (transferring less energy to the *type-I* mode and changing sign, thus becoming a disruptive term, for the *type-II* modes) for the weaker CFV flow-field. The Reynolds stresses related to the wall-normal shears transferred less energy from the *type-I* mode and did not change their effect on the *type-II* mode, when comparing the weaker to the stronger vortex base-flow. From the current measurements, Reynolds stresses are obviously not accessible. Despite this, the spanwise and wall-normal velocity gradients for the two stationary vortices can be compared. This is done in figure 16, confirming the strong reduction of the spanwise shears (in the outer upwelling air region pertaining to *type-I* mode) and the weak modification of the wall-normal gradient (on the top region of the stationary wave) for the weaker vortex thus partially confirming the analysis of Groot et al. [12]. Furthermore, the POD analysis performed by Serpieri and Kotsonis[32] on the stronger CFV and leading to the individuation of the flow structures of both *type-I* and *type-III* modes did not yield the same clear results on the weaker CFV considered in this section.

The results presented in this section show the strong dependence of the unsteady field on the underlying stationary flow. This effect was investigated in numerical simulations by Wassermann and Kloker [35] and recently by Choudhari et al. [5] and Groot et al. [12] and here experimentally reconciled.

4.6. Effect of actuator location

The actuator was installed at a more downstream position ($x/c = 0.375$) to investigate the effect that this has on the flow development. The larger amplitude stationary vortex is considered for this analysis. In figure 17, the spatial evolution of the stationary and unsteady modes is plotted for the unforced and for the low-frequency forcing case. The evolution of the stationary mode is comparable to the one observed in figure 9 (these measurements

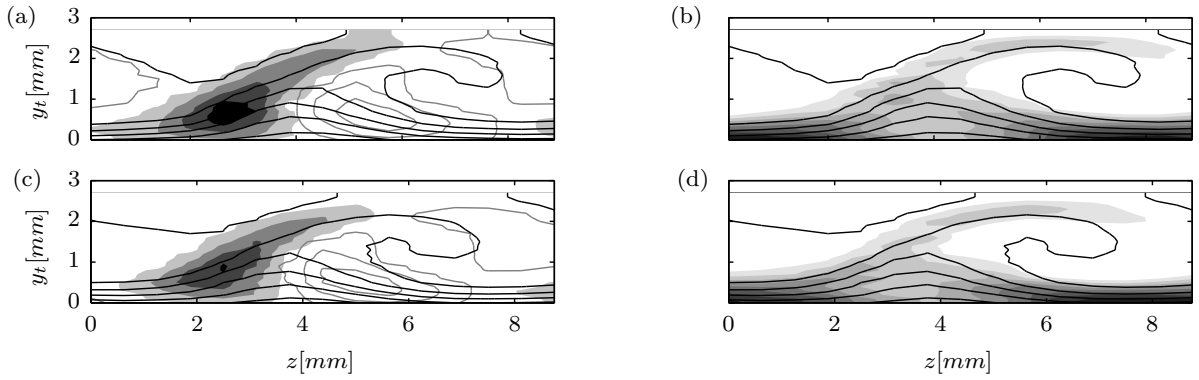

Figure 16: (a and c) non-dimensional spanwise velocity gradient $((\partial|\bar{V}^{HWA}|/\partial z)/(|\bar{V}_e^{HWA}|/\lambda_z))$ (10 levels, shaded: between -37.4 and -3.74; grey solid lines: between 3.74 and 37.4); (b and d) non-dimensional wall-normal velocity gradient $(\partial|\bar{V}^{HWA}|/\partial y_t/(|\bar{V}_e^{HWA}|/\lambda_z))$ (10 levels, shaded from 20.79 to 207.9). (a and b) stronger CFV; (c and d) reduced amplitude CFV. Black line contours denote time averaged velocity.

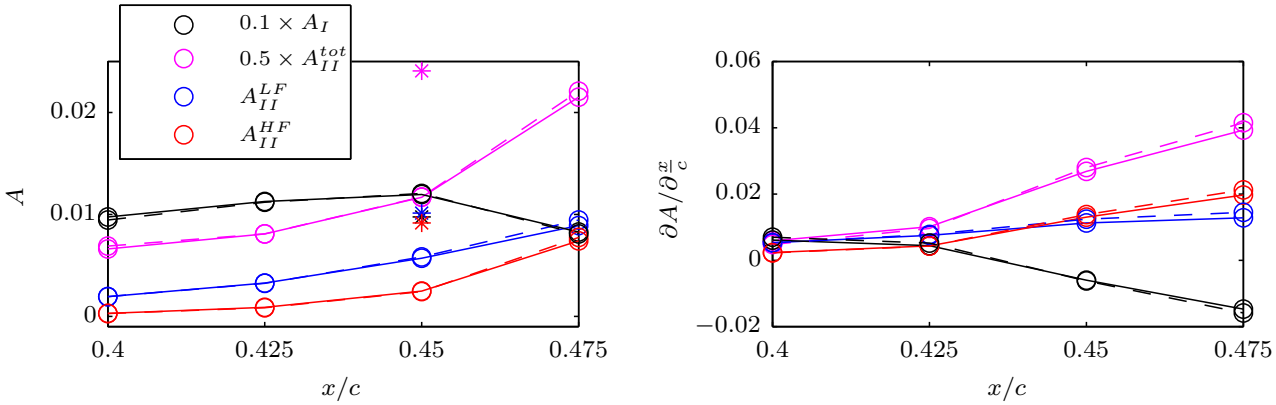

Figure 17: Same caption as figure 9. Actuator installed at $x/c = 0.375$, larger amplitude stationary vortex.

encompass the same stationary vortex) showing that the actuator, when not operated has negligible effect on the boundary layer. Also for this case, the CFV appears practically unaffected by the 400Hz actuation. The unsteady modes present instead some differences compared to the case of the actuator at $x/c = 0.30$ especially at station $x/c = 0.45$. Overall, the low-frequency forcing does not strongly change the flow, similarly to the upstream forcing location results. In contrast, the higher frequency forcing considerably enhances the full-spectrum fluctuations as well as the high and low-frequency bands with the latter overtaking the former.

In order to gauge this effect, the boundary layer status is inferred by inspection of the statistical velocity fields for the three flow cases (unforced, low- and high-frequency actuation), shown in figure 18. While the low-frequency actuation does not show evident effects on the flow field, the high-frequency forcing triggers the breakdown of the stationary vortex with a broad area of high energy fluctuations spreading from the upwelling flow region (pertinent of the *type-I* mode) and merging with the inner vortex leg (where mode *type-III* develops) thus explaining the reported increased amplitude of both the high- and low-frequency. A further consequence of the onset of flow breakdown by the high-frequency actuation is that the amplitude of the phase reconstructed fluctuations drops to $A_{II}^{PR} = 0.0016$ which is four times smaller than the same quantity measured with the actuator placed at $x/c = 0.30$ (see table 2). Therefore the phase-reconstruction procedure for this flow field yields less clear results. These observations show that high-frequency forcing at the downstream position ($x/c = 0.375$) anticipates the flow breakdown with the related enhancement and spreading, in both space and frequency band of the unsteady field. This lies in contrast to the flow development when forcing is applied at $x/c = 0.3$.

A possible route to the more advanced transition process when downstream forcing is applied, can be sought by considering the stability and growth characteristics of secondary cross-flow instabilities. To this end, hot-wire measurements from the experiment by Serpieri and Kotsonis [32] are used. In figure 19, the chordwise evolution of the high and low-frequency bands are measured according to equation 4. As said, the same flow case was consid-

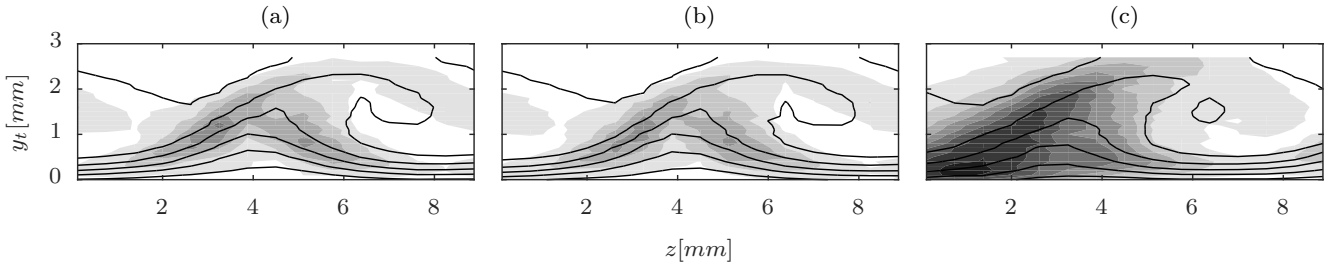

Figure 18: Time-averaged velocity fields (solid lines: 7 levels, from 0 to $|\bar{V}_e^{HWA}|$) and velocity fluctuation fields (shaded: 10 levels, from 0 to $0.16|\bar{V}_e^{HWA}|$) at $x/c = 0.45$, larger amplitude stationary vortex. AC-DBD actuator installed at $x/c = 0.375$: (a) non-operative; (b) $f_{DBD} = 0.4$kHz - $E = 1.5k$V; (c) $f_{DBD} = 4$kHz - $E = 1.2$kV.

ered in [32], albeit no plasma actuators were installed on the wing surface. The velocity fields pertaining to three stationary vortices were measured and averaged ($z^m = 3 \times \lambda_z = 27$mm). The amplitudes are plotted in logarithmic scale to facilitate comparison of more upstream portions of the plot where the chordwise amplitudes of the high-frequency mode evolve slowly. Figure 19 shows that the high-frequency fluctuations, pertinent to the *type-I* mode forced in this study (denoted by the HF notation), undergo abrupt growth from $x/c = 0.40$ while showing a rather flat amplitude evolution at the more upstream stations. Considering the sensitivity associated to HWA, amplitudes of $A < 10^{-4}$ can be considered as basically undetected (similar to the observations of [38]). This further suggests that the boundary layer is only mildly unstable or even stable to high-frequency secondary instabilities up to $x/c = 0.375 - 0.40$, for the conditions of this experiment. The implication of this observation, reconciles the behaviour of the presently studied flow under forcing at two different streamwise positions. Based on figure 19, an actuator which is forcing at $x/c = 0.3$ would introduce secondary instabilities that need to travel a longer 'stable' region than an actuator placed at $x/c = 0.375$. Consequently, the instabilities forced by the upstream actuator would reach branch-I ($x/c \approx 0.4$) at a relatively lower amplitude than the instabilities forced by the downstream actuator. Naturally, the aforementioned considerations pertain to forcing of equal initial amplitude. In absolute terms, this is the case for the present study as both voltage and frequency are kept constant for the two actuator positions. However, in momentum coefficient terms, the downstream actuator effect is even weaker (section 2.3), as, moving downstream, the local boundary layer becomes thicker and the external velocity higher. This further confirms that the observed flow-field changes under downstream forcing are related to the reduced stability of the flow to secondary instabilities at this position, compared to upstream forcing.

The outcomes of this section suggest that a careful characterization of the unforced transitional boundary layer is needed for studies based on forcing of secondary modes as, even weak actuated disturbance, can cause flow breakdown if occurring close to the natural critical location [13, 34]..

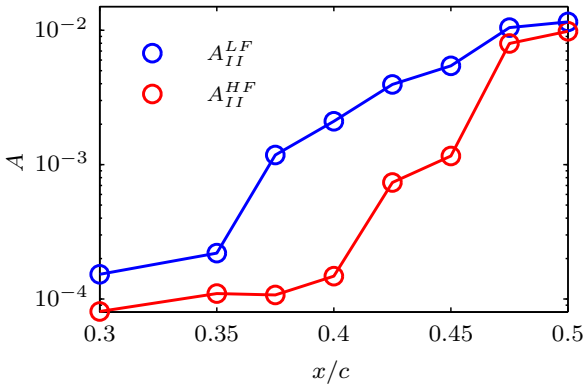

Figure 19: Chordwise evolution of fluctuation amplitudes (see equations 4) (logarithmic scale). Data from the experiment by Serpieri and Kotsonis [32]. HF and LF bands are the same of figure 8. Unforced flow without AC-DBD plasma actuator mounted.

5. Conclusions

Unsteady low- and high-frequency instability modes arising at the last stages of transition in the pressure side boundary layer of a 45° swept wing have been experimentally investigated. The Reynolds number of the experiment was $Re = 2.17 \cdot 10^6$ and the wing was set at small incidence to enhance the cross-flow instability mechanisms. Primary stationary cross-flow instability was forced to the most amplified mode by means of micron-sized roughness elements near the leading edge. Building upon previous work by Kawakami et al., Deyhle and Bippes and White and Saric [38], the measurement technique employed in this study is hot-wire anemometry. Scans along planes aligned with the wall-normal-spanwise directions, at different chordwise stations were performed using an automated traversing support of the hot-wire probe.

Unsteady periodic forcing of the *type-I* and *type-III* modes was performed by means of an AC-DBD plasma actuator flush mounted to the model surface. The actuator

was installed upstream of the measurement domain and consisted of a very thin strip of silver-printed electrodes, summing up to a two-dimensional roughness of 125μm. The actuator was operated at two different frequencies of $f_{DBD} = 0.4$kHz and $f_{DBD} = 4$kHz respective of the two analysed modes. The voltage amplitude was varied with the frequency and set such to minimize the effects on the transition pattern. Nonetheless, when forcing was applied upstream of *type-I mode* branch-I, it demonstrated the capability of weekly enhancing and narrowing the spectral distribution of the forced modes. Finally, through the deterministic nature of the applied forcing, the phase of the triggered modes was successfully conditioned. The actuator signal was acquired simultaneously with the hot-wire and used to reconstruct, by means of phase averaging, the measured signals. This procedure allowed the inspection of the spatio-temporal evolution of both the low (*type-III*) and high (*type-I*) frequency modes. The presented results are in good agreement with results of previous attempts to force the secondary instability modes, by means of localized periodic blowing/suction, by Kawakami et al. [14], Chernoray et al. [4] and van Bokhorst and Atkin [34]. The results further show that AC-DBD plasma actuators are suitable for this type of investigations. While avoiding three-dimensional artefacts, given their spanwise uniformity, the inherent body force production mechanisms of these actuators cause a modulation of the reconstructed modes, which needs to be taken into account. They can be operated at different frequencies (an order of magnitude apart in the current study) and their authority is easily adjusted by tuning the amplitude of the supplied voltage. Finally, the possibility of directing the forced jets along a specific direction becomes crucial in applications where flows are undergoing strong distortions.

The outcomes of the phase-reconstruction analysis agree with the previous efforts in understanding the mechanisms leading to the breakdown of swept wing boundary layers, providing an experimental companion to the numerical investigations of Högberg and Henningson [13] and Wassermann and Kloker [35], and the theoretical work of Malik et al. [22], Fischer and Dallmann [10] and Bonfigli and Kloker [3]. Finally the current results offer a validation of the recent tomographic PIV experiment performed by the same authors of this study [32].

Two different cross-flow vortices of different amplitude (about ten percent difference in the mode shape amplitude defined in equation 3) were measured showing the influence on the development of secondary modes: the weaker wave is shown to be more stable to the unsteady disturbances especially under high-frequency forcing. This results are in line with the simulations of Wassermann and Kloker [35] and Choudhari et al. [5] and the stability computations of Groot et al. [12]. At these conditions, the high-frequency phase-correlated fluctuations become significantly weaker thus not allowing a clear representation of their topology and evolution. Finally, the effect of the actuator position was investigated. Placing the actuator more downstream and operating it at the higher frequency triggered the laminar-to-turbulent breakdown of the boundary layer. This effect was shown to be caused by the boundary layer stability characteristics to secondary mechanisms.

Acknowledgments

This research is funded by the Netherlands Organisation for Scientific Research *NWO-STW* under the *Veni* grant. The authors are thankful to Koen Groot for valuable discussions and to the anonymous referees for their valuable comments.

References

[1] Arnal, D., Gasparian, G., and Salinas, H. (1998). Recent advances in theoretical methods for laminar-turbulent transition prediction. *AIAA* Paper 1998-0223.

[2] Bippes, H. (1999). Basic experiments on transition in three-dimensional boundary layers dominated by crossflow instability. *Progress in Aerospace Sciences*, 35(4):363 – 412.

[3] Bonfigli, G. and Kloker, M. (2007). Secondary instability of crossflow vortices: validation of the stability theory by direct numerical simulation. *J. Fluid Mech.*, 583:229–272.

[4] Chernoray, V. G., Dovgal, A. V., Kozlov, V. V., and Löfdahl, L. (2005). Experiments on secondary instability of streamwise vortices in a swept-wing boundary layer. *J. Fluid Mech.*, 534:295–325.

[5] Choudhari, M. M., Li, F., and Paredes, P. (2016). Influence of stationary crossflow modulation on secondary instability. *AIAA Paper* 2016-3788.

[6] Corke, T. C., Enloe, C. L., and Wilkinson, S. P. (2010). Dielectric barrier discharge plasma actuators for flow control. *Annu. Rev. Fluid Mech.*, 42:505–529.

[7] Deyhle, H. and Bippes, H. (1996). Disturbance growth in an unstable three-dimensional boundary layer and its dependence on environmental conditions. *J. Fluid Mech.*, 316:73–113.

[8] Dörr, P. and Kloker, M. (2015). Numerical investigation of plasma-actuator force-term estimations from flow experiments. *Journal of Physics D: Applied Physics*, 48(39):395203.

[9] Dörr, P. and Kloker, M. (2016). Transition control in a three-dimensional boundary layer by direct attenuation of nonlinear crossflow vortices using plasma actuators. *International Journal of Heat and Fluid Flow*, pages 449–465.

[10] Fischer, T. M. and Dallmann, U. (1991). Primary and secondary stability analysis of a three-dimensional boundary-layer flow. *Physics of Fluids A: Fluid Dynamics (1989-1993)*, 3(10):2378–2391.

[11] Glauser, M. N., Saric, W. S., Chapman, K. L., and Reibert, M. S. (2014). Swept-wing boundary-layer transition and turbulent flow physics from multipoint measurements. *AIAA Journal*, 52(2):338–347.

[12] Groot, K., Serpieri, J., Pinna, F., and Kotsonis, M. (under review). Secondary crossflow instability through biglobal analysis of measured base flows. *J. Fluid Mech.*

[13] Högberg, M. and Henningson, D. (1998). Secondary instability of cross-flow vortices in falkner-skan-cooke boundary layers. *J. Fluid Mech.*, 368:339–357.

[14] Kawakami, M., Kohama, Y., and Okutsu, M. (1999). Stability characteristics of stationary crossflow vortices in three-dimensional boundary layer. *AIAA* Paper 1998-811.

[15] Koch, W., Bertolotti, F. P., Stolte, A., and Hein, S. (2000). Nonlinear equilibrium solutions in a three-dimensional boundary layer and their secondary instability. *J. Fluid Mech.*, 406:131–174.

[16] Kohama, Y., Saric, W. S., and Hoos, J. A. (1991). A high frequency secondary instability of crossflow vortices that leads to transition. *Proc. R. Aeronaut. Soc. Conf. on Boundary-Layer Transition and Control,* Cambridge, UK.

[17] Kotsonis, M. (2015). Diagnostics for characterisation of plasma actuators. *Measurement Science and Technology*, 26(9):092001.
[18] Kotsonis, M. and Ghaemi, S. (2011). Forcing mechanisms of dielectric barrier discharge plasma actuators at carrier frequency of 625 hz. *Journal of Applied Physics*, 110(11):113301.
[19] Kotsonis, M., Giepman, R., Hulshoff, S., and Veldhuis, L. (2013). Numerical study of the control of tollmien–schlichting waves using plasma actuators. *AIAA Journal*, 51(10):2353–2364.
[20] Kotsonis, M. and Veldhuis, L. (2010). Experimental study on dielectric barrier discharge actuators operating in pulse mode. *Journal of Applied Physics*, 108(11).
[21] Malik, M. R., Li, F., and Chang, C.-L. (1994). Crossflow disturbances in three-dimensional boundary layers: nonlinear development, wave interaction and secondary instability. *J. Fluid Mech.*, 268:1–36.
[22] Malik, M. R., Li, F., Choudhari, M., and Chang, C.-L. (1999). Secondary instability of crossflow vortices and swept-wing boundary-layer transition. *J. Fluid Mech.*, 399:85–115.
[23] Michelis, T., Yarusevych, S., and Kotsonis, M. (2017). Response of a laminar separation bubble to impulsive forcing. *J. Fluid Mech.*, 820:633–666.
[24] Moreau, E. (2007). Airflow control by non-thermal plasma actuators. *Journal of Physics D: Applied Physics*, 40(3):605.
[25] Pereira, R., Ragni, D., and Kotsonis, M. (2014). Effect of external flow velocity on momentum transfer of dielectric barrier discharge plasma actuators. *Journal of Applied Physics*, 116(10).
[26] Poll, D. I. A. (1985). Some observations of the transition process on the windward face of a long yawed cylinder. *J. Fluid Mech.*, 150:329–356.
[27] Reibert, M. S., Saric, W. S., Carrillo, R. B. J., and Chapman, K. (1996). Experiments in nonlinear saturation of stationary crossflow vortices in a swept-wing boundary layer. *AIAA* Paper 1996-0184.
[28] Saddoughi, S. G. and Veeravalli, S. V. (1996). Hot-wire anemometry behaviour at very high frequencies. *Measurement Science and Technology*, 7(10):1297–1300.
[29] Saric, W. S., Reed, H. L., and White, E. B. (2003). Stability and transition of three-dimensional boundary layers. *Annu. Rev. Fluid Mech.*, 35(1):413–440.
[30] Schlichting, H. and Gersten, K. (2000). *Boundary layer theory*. Number 390. Cambridge University Press.
[31] Serpieri, J. and Kotsonis, M. (2016a). Spatio-temporal characteristics of secondary instabilities in swept wing boundary layers. *AIAA* Paper 2016-3792.
[32] Serpieri, J. and Kotsonis, M. (2016b). Three-dimensional organisation of primary and secondary crossflow instability. *J. Fluid Mech.*, 799:200–245.
[33] Serpieri, J., Yadala Venkata, S., and Kotsonis, M. (2017). Conditioning of cross-flow instability modes using dielectric barrier discharge plasma actuators. *J. Fluid Mech.*, 833:164–205.
[34] van Bokhorst, E. and Atkin, C. J. (2017). Wall forcing of the secondary crossflow instability. *AIAA Paper* 2017-3458.
[35] Wassermann, P. and Kloker, M. (2002). Mechanisms and passive control of crossflow-vortex-induced transition in a three-dimensional boundary layer. *J. Fluid Mech.*, 456:49–84.
[36] Wassermann, P. and Kloker, M. (2003). Transition mechanisms induced by travelling crossflow vortices in a three-dimensional boundary layer. *J. Fluid Mech.*, 483:67–89.
[37] Welch, P. D. (1967). The use of fast fourier transform for the estimation of power spectra: A method based on time averaging over short, modified periodograms. *Audio and Electroacoustics, IEEE Transactions on*, 15(2):70–73.
[38] White, E. B. and Saric, W. S. (2005). Secondary instability of crossflow vortices. *J. Fluid Mech.*, 525:275–308.
[39] Yarusevych, S. and Kotsonis, M. (2017). Steady and transient response of a laminar separation bubble to controlled disturbances. *J. Fluid Mech.*, 813:955–990.